

## Supporting Information

### Effect of S··· $\pi$ interaction on charge transport properties of DPP framework

Xu Wang, Zhonghao Hu, Lei Liang, Zhiye Wang, Yanze Wang, Yunchuan Li\*, Bohuai Xiao\*

The State Key Laboratory of Refractories and Metallurgy, Faculty of Materials, Wuhan University of Science and Technology, Wuhan 430081, China.

\*Corresponding authors. Emails: yc.l@wust.edu.cn (Y.L.); xiaobhuai@foxmail.com (B.X.);

#### Table of Contents

S1. Synthetic routes and characterization.....	S-2
S2. Conductance measurements of single-molecule junction.....	S-4
S3. The single-molecule conductance for DPP-R and DPP-B.....	S-5
S4. Optimization and analysis of molecular structures.....	S-7
S5. Cyclic voltammetry (CV), absorption spectrum and energy level.....	S-7
S6. AIM analysis by Multiwfn.....	S-8
S7. Summary of the photophysical and electrochemical.....	S-8
S8. Cyclic voltammetry and Mulliken charge density of DPP-R and DPP-B.....	S-8
S9. Au-S binding configuration and transmission pathway.....	S-9

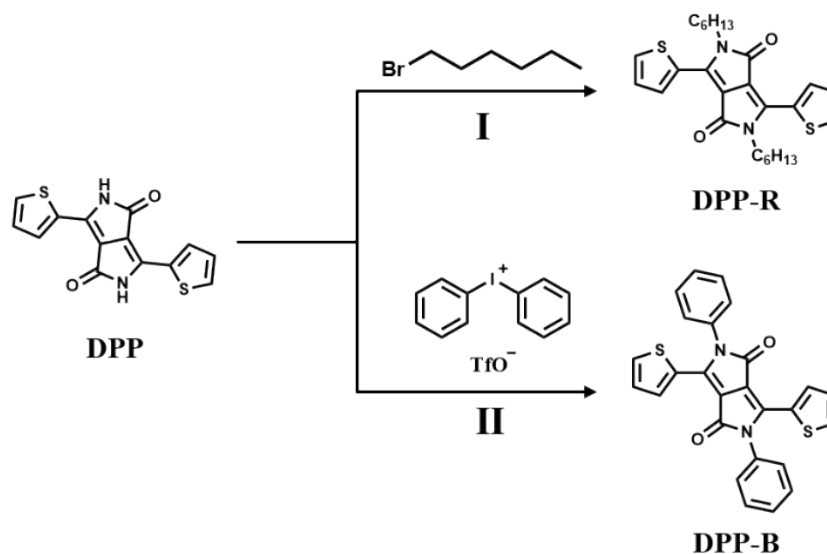
## General information

$^1\text{H}$  NMR &  $^{13}\text{C}$  NMR spectra were acquired on a Bruker NMR spectrometer operating at 600 and 150 MHz, respectively, with samples dissolved in Chloroform-*d* using tetramethylsilane (TMS) as an internal standard. MALDI-TOF (matrix-assisted laser-desorption/ionization time-of-flight) mass spectra were performed on a Bruker BIFLEXIII TOF mass spectrometer. UV-vis absorption was measured on a Shimadzu UV-2000. Cyclic voltammetry (CV) was performed on a CHI600D electrochemical workstation with a glassy carbon working electrode and a Pt wire counter electrode at a scanning rate of  $0.05\text{ V}\cdot\text{s}^{-1}$  against a Ag/AgCl reference electrode in dichloromethane and tetrabutylammonium hexafluorophosphate of  $0.1\text{ mol}\cdot\text{L}^{-1}$  as supporting electrolyte under Nitrogen bubbling. Materials, including solvents and chemicals were used without further purification after purchasing from commercial suppliers.

Single molecular conductance measurements were carried out with a home-built z-axis STM. The initial approach of the gold tip to the substrate was sequentially controlled by a stepper Picomotor (Newport 8742-4-KIT, Germany, minimum displacement increment is less than 30 nm) and a 1-axis piezo actuator (S-303.0L PI, Germany, the spatial resolution is 0.03 nm). During the STM-BJ experiments, the tip movement is only controlled by the piezo. To achieve a high spatial resolution, the voltage output to the piezo is provided by a NI PXIe-4463 card (24 bits) in the range of -10 V to 10 V without amplification. The voltage output from the DAQ card has a resolution of 10  $\mu\text{V}$ , resulting in a piezo displacement resolution of 0.03 nm. A NI PXIe-4309 (18 bits at 2 MS/s/ch) is used to record the current, which is first amplified by a variable range current-voltage converter (DLPCA-200, Femto, Germany, current sensitivity of preamplifier is  $10^{-3} \sim 10^{-11}\text{ A/V}$ ). A custom LabVIEW program is coded to run the system, including hardware controlling and data acquisition.

## S1 Synthetic routes and characterization

The preparing process of DPP-R and DPP-B were as follows (Scheme. S1):



Reagents and conditions: (I)  $\text{K}_2\text{CO}_3$ , DMF, 105-110  $^\circ\text{C}$ , 1-bromohexane, 110  $^\circ\text{C}$ , overnight. (II) CuI,  $\text{K}_2\text{CO}_3$ , DMF, 130  $^\circ\text{C}$ , 12h, air.

Scheme. S1 Synthetic routes of DPP-R and DPP-B.<sup>1,2</sup>

### 2,5-dihexyl-3,6-di(thiophen-2-yl)-2,5-dihydropyrrolo[3,4-c]pyrrole-1,4-dione (DPP-R)

3,6-di(thiophen-2-yl)-2,5-dihydropyrrolo[3,4-c]pyrrole-1,4-dione (DPP) (450 mg, 1.5 mmol) and anhydrous  $\text{K}_2\text{CO}_3$  (790 mg, 5.7 mmol) were dissolved in dry DMF (16 mL) and heated to 105 - 110  $^\circ\text{C}$  under argon. 1-bromohexane (7.65 g, 43 mmol) was added and the mixture was stirred overnight at 110  $^\circ\text{C}$ . The mixture was poured into cold water and extracted with dichloromethane (DCM). The DCM layer was collected and dried over anhydrous  $\text{MgSO}_4$ . The reaction mixture was concentrated in vacuo and purified by flash column chromatography on silica gel. DPP-R was obtained as a dark purple solid (340 mg, 48%).  $^1\text{H}$  NMR (600 MHz, Chloroform-*d*)  $\delta$  8.92 (dd,  $J = 3.9, 1.2\text{ Hz}$ , 2H), 7.64 (dd,  $J = 5.0, 1.1\text{ Hz}$ , 2H), 7.31 - 7.26 (m, 2H), 4.10 - 4.04 (m, 4H), 1.74 (ddd,  $J = 12.4, 10.0, 6.5\text{ Hz}$ , 4H), 1.41 (dt,  $J = 10.6, 6.9\text{ Hz}$ , 4H), 1.32 (dq,  $J = 6.3, 3.1, 2.7\text{ Hz}$ , 8H), 0.91 - 0.85 (m, 6H).  $^{13}\text{C}$  NMR (151 MHz, Chloroform-*d*)  $\delta$  161.32, 139.97, 135.23, 130.63, 129.76, 128.57, 107.66, 42.19, 31.38, 29.89, 26.52, 22.53, 13.98. HR-MS (MALDI-TOF): calcd. for  $\text{C}_{26}\text{H}_{33}\text{N}_2\text{O}_2\text{S}_2$   $[\text{M}+\text{H}]^+$  469.1983; Found: 469.1980.

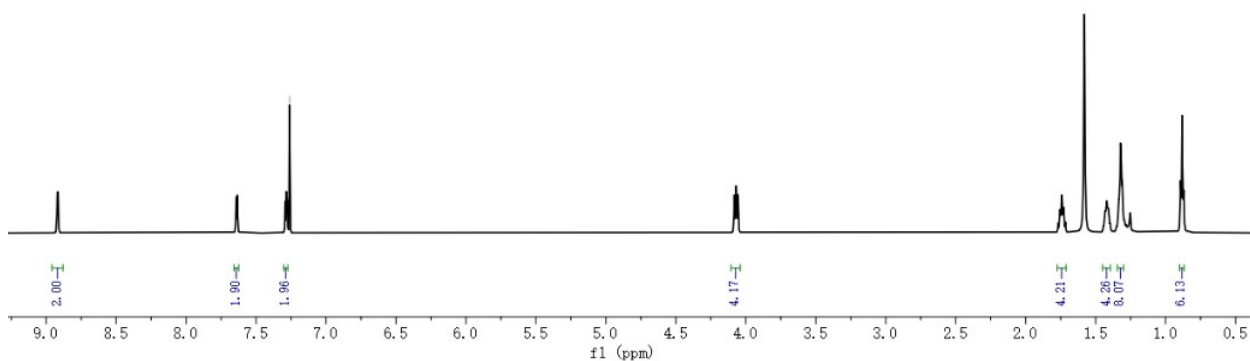


Fig. S1  $^1\text{H}$  NMR spectra of DPP-R in  $\text{CDCl}_3$ .

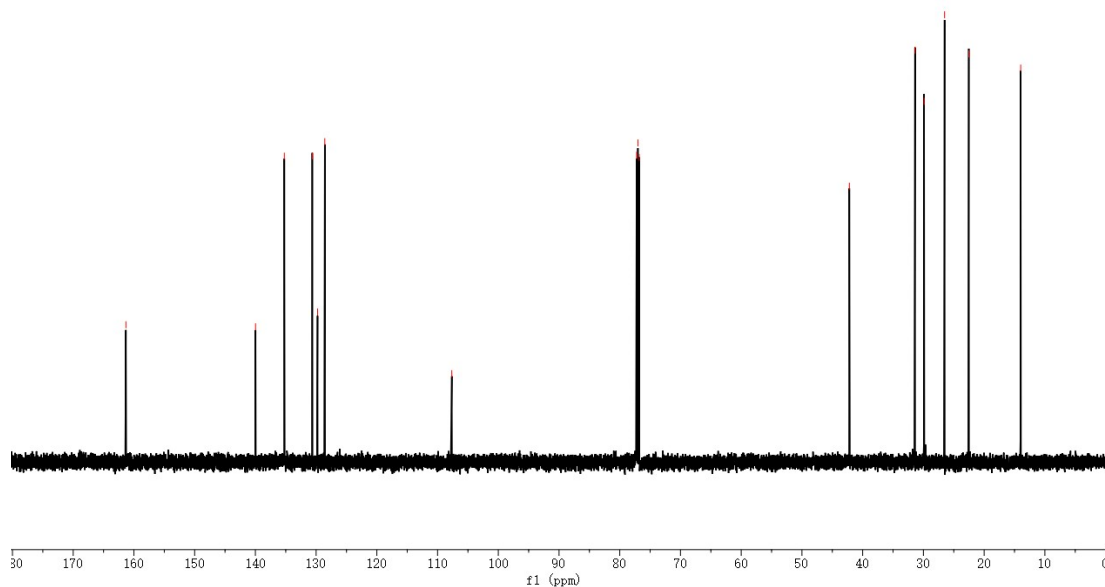


Fig. S2  $^{13}\text{C}$  NMR spectra of DPP-R in  $\text{CDCl}_3$ .

### 2,5-diphenyl-3,6-di(thiophen-2-yl)-2,5-dihydropyrrolo[3,4-c]pyrrole-1,4-dione (DPP-B)

To a Schlenk tube equipped with a magnetic stir bar was charged with DPP (200 mg, 0.67 mmol), Diphenyliodonium triflate (860 mg, 2 mmol), CuI (26 mg, 0.136 mmol),  $\text{K}_2\text{CO}_3$  (276 mg, 2 mmol), 4,4'-di-tert-butyl-2,2'-bipyridine (72 mg, 0.268 mmol) and DMF (50 mL). The mixture was stirred at 130  $^\circ\text{C}$  for 12 h in air. The reaction mixture was concentrated in vacuo and purified by flash column chromatography on silica gel. DPP-B was obtained as a red solid (39 mg, 13%).  $^1\text{H}$  NMR (600 MHz, Chloroform-*d*)  $\delta$  8.80 (d,  $J = 3.9$  Hz, 2H), 7.58 – 7.54 (m, 6H), 7.45 – 7.39 (m, 6H), 7.10 (t,  $J = 4.5$  Hz, 2H).  $^{13}\text{C}$  NMR (151 MHz, Chloroform-*d*)  $\delta$  161.54, 140.10, 135.60, 134.99, 132.11, 130.32, 130.15, 129.83, 129.63, 127.92, 107.52. HR-MS (MALDI-TOF): calcd. for  $\text{C}_{26}\text{H}_{17}\text{N}_2\text{O}_2\text{S}_2$   $[\text{M}+\text{H}]^+$  453.0731; Found: 453.0729.

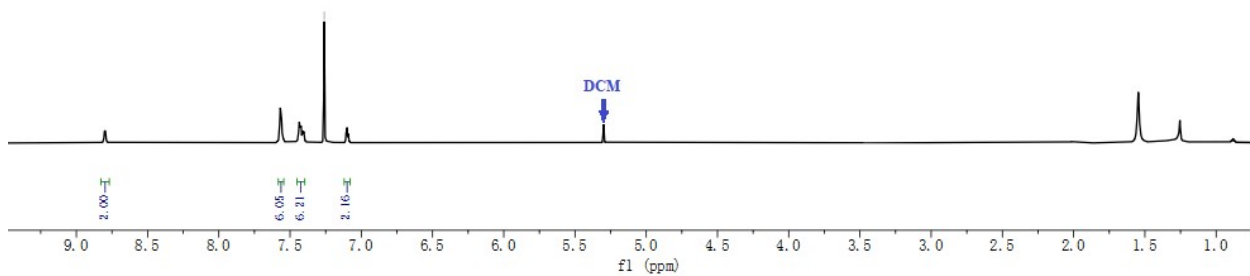


Fig. S3  $^1\text{H}$  NMR spectra of DPP-B in  $\text{CDCl}_3$ .

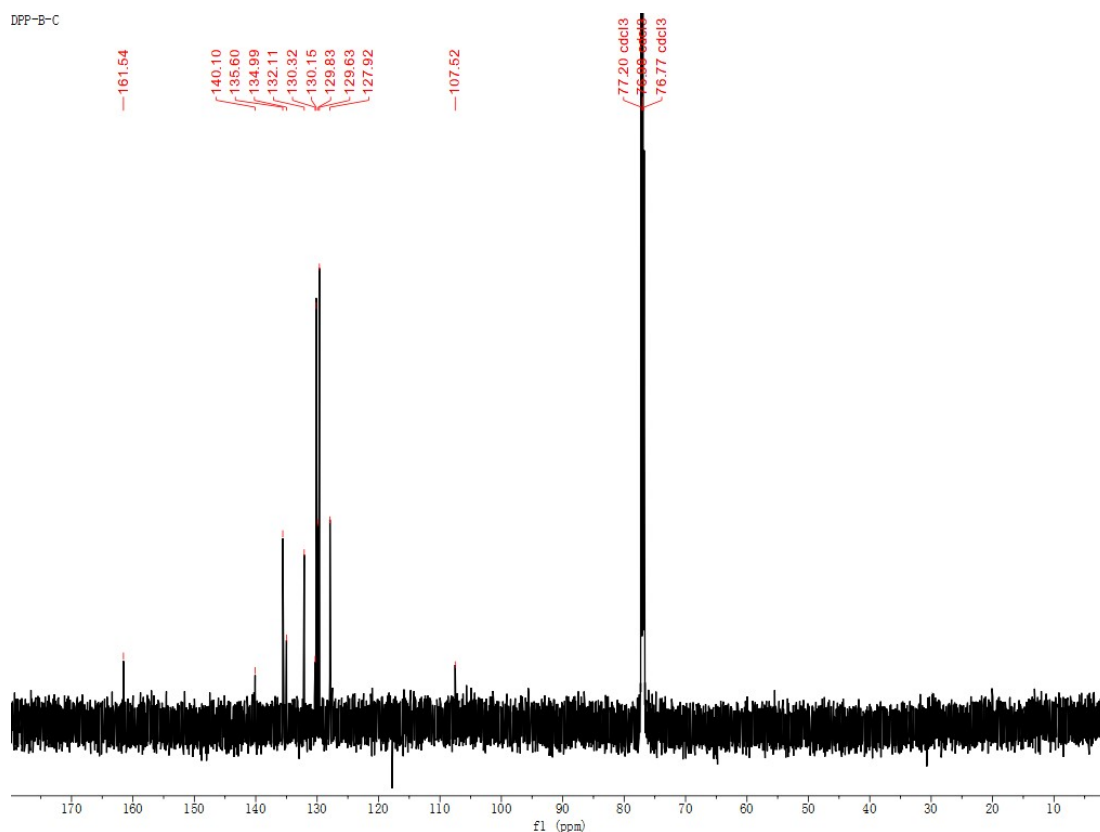


Fig. S4  $^{13}\text{C}$  NMR spectra of DPP-B in  $\text{CDCl}_3$ .

## S2 Conductance measurements of single-molecule junction.

### S2.1 Preparation of test samples

The DPP-R and DPP-B molecules were dissolved in 1,2,4-trichlorobenzene (99.99%, Sigma-Aldrich, USA), followed by sonication for 15 min to dissolve them completely and prepared to 1 mM solutions of DPP-R and DPP-B molecules for subsequent single-molecule conductance measurements.

### S2.2 Preparation of nano electrodes

The Au tip electrodes were prepared by electrochemical etching using a 1:1 volume ratio of hydrochloric acid and anhydrous ethanol, followed with piranha solution (concentrated sulfuric acid and hydrogen peroxide uniformly mixed in a 3:1 volume ratio), ultrapure water and anhydrous ethanol to remove the oxide impurities and residual etching solution generated during the preparation process. The Au substrates were prepared by sequentially vaporizing 20 nm Cr and 100 nm Au on clean silicon wafers by a vacuum thermal evaporation coater (Covap, Angstrom Engineering, Canada).

### S2.3 Single-molecule conductance measurement

The DPP-R (1 mM) or DDP-B (1 mM) solution was added dropwise onto the Au substrate. Prior to data collection, the STM setup was warmed up and stabilized for at least 30 min. The STM-BJ experiments are controlled by a custom LabVIEW program. The tip is

repeatedly approached and then retracted from the substrate at a speed of 20 nm/s with a constant bias of 0.1 V. During each cycle, the tip contacts the substrate and then withdraws a distance of 20 nm. The recorded  $G$ - $D$  curves are analysed by a custom LabVIEW program.

### S3 The single-molecule conductance for DPP-R and DPP-B.

#### S3.1 The conductance of DPP-R and DPP-B with current amplifier of $10^6 \text{ V}\cdot\text{A}^{-1}$

The single-molecule conductance of DPP-R and DPP-B was measured with current amplifier of  $10^6 \text{ V}\cdot\text{A}^{-1}$ , with gold quantum conductance ( $G_0$ ) plateaus signal indicated in Fig. S5. The obtained 1D conductance histogram (Fig. S5c and d) is consistent with the results measured using a current amplifier of  $10^7 \text{ V}\cdot\text{A}^{-1}$ .

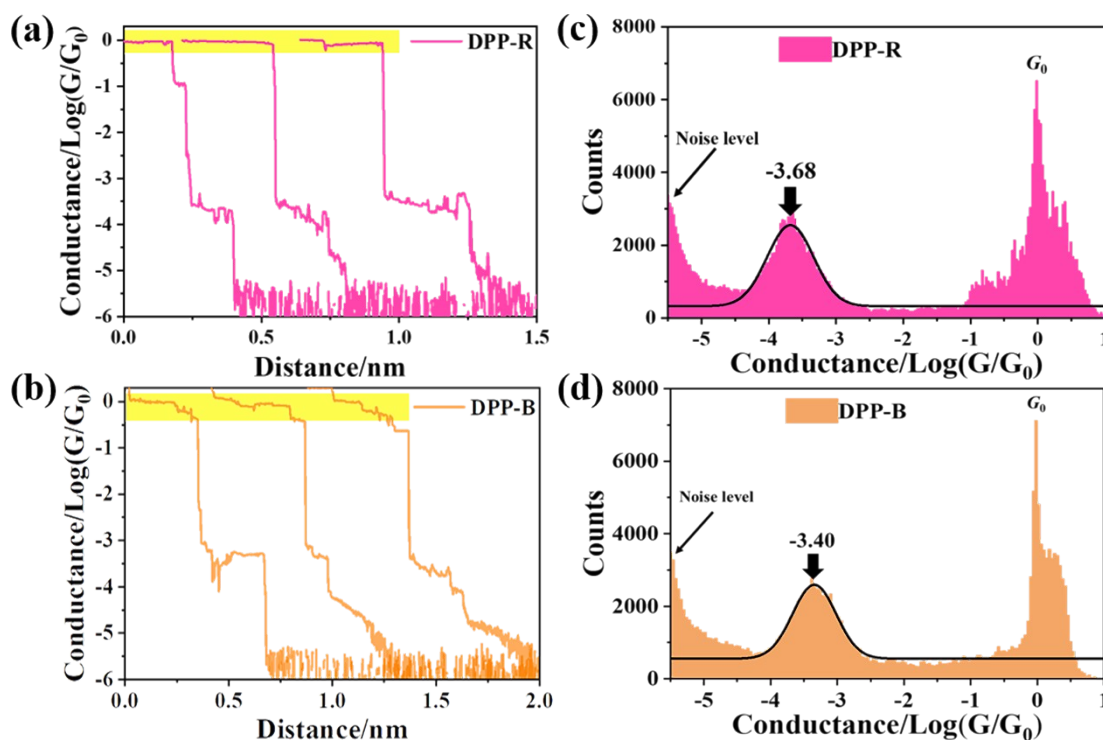


Fig. S5 (a-b) Typical Conductance-Distance curves of DPP-R and DPP-B in TCB. (c-d) Conductance histograms of DPP-R and DPP-B in TCB.

#### S3.2 The conductance of DPP-R and DPP-B in 1,3,5-Trimethylbenzene (TMB).

We performed conductance measurements with TMB (1,3,5-trimethylbenzene) substituted for TCB (1,2,4-trichlorobenzene) with current amplifier of  $10^6 \text{ V}\cdot\text{A}^{-1}$ . The results (as shown in the Fig. S6) show that DPP-R and DPP-B has almost the same conductance difference in TMB as in TCB, as shown in the Table. S1.

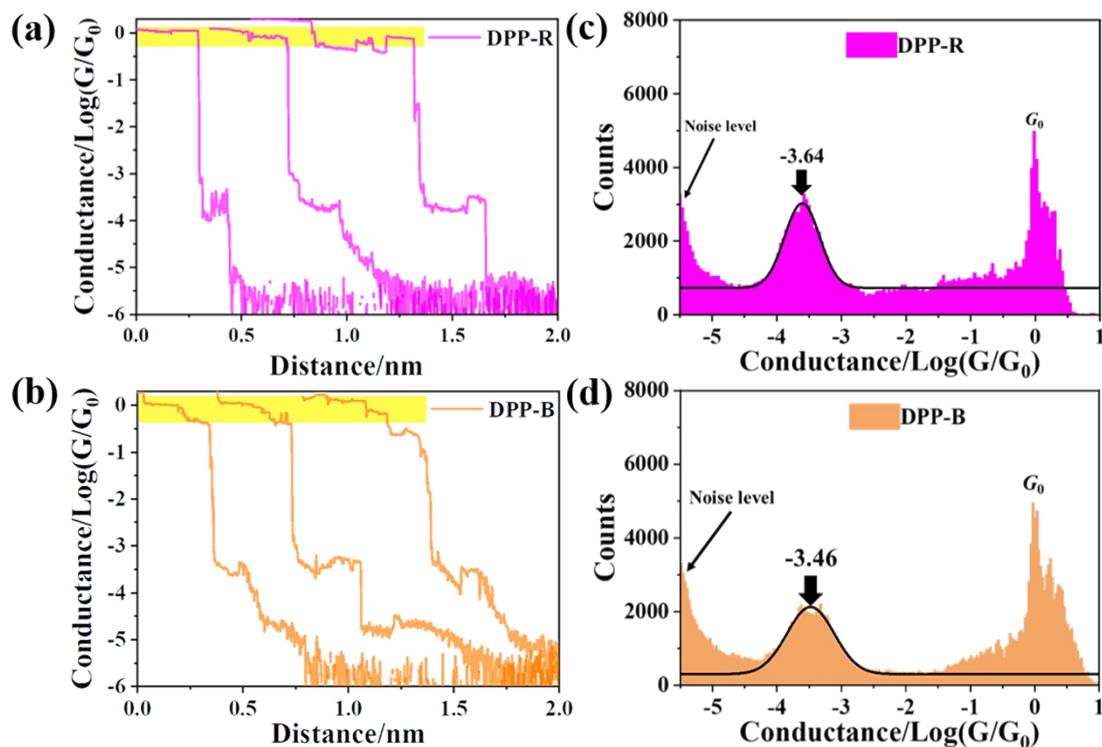


Fig. S6 (a-b) Typical Conductance-Distance curves of DPP-R and DPP-B in TMB. (c-d) Conductance histograms of DPP-R and DPP-B in TMB.

Table. S1 Conductance results of DPP-R and DPP-B in different solvents.

Molecule	Conductance/Log(G/G <sub>0</sub> )	
	TCB	TMB
DPP-R	-3.68 ± 0.0073	-3.64 ± 0.00479
DPP-B	-3.40 ± 0.00579	-3.46 ± 0.00633

### S3.3 The conductance of DPP-R at different concentrations in TCB.

Previous studies have reported the molecular junction with long alkyl side chain exhibit a concentration dependence bimodal conductance,<sup>3</sup> so we conducted STM-BJ experiment to investigate the concentration dependence of DPP-R (n-hexyl as side chain) molecular junction. As shown in Fig. S7, different concentrations do not lead to significant change in conductance of DPP-R.

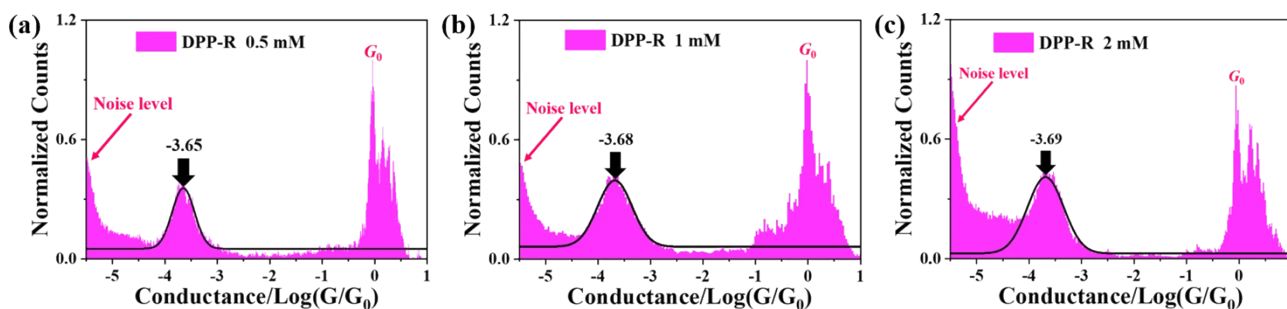
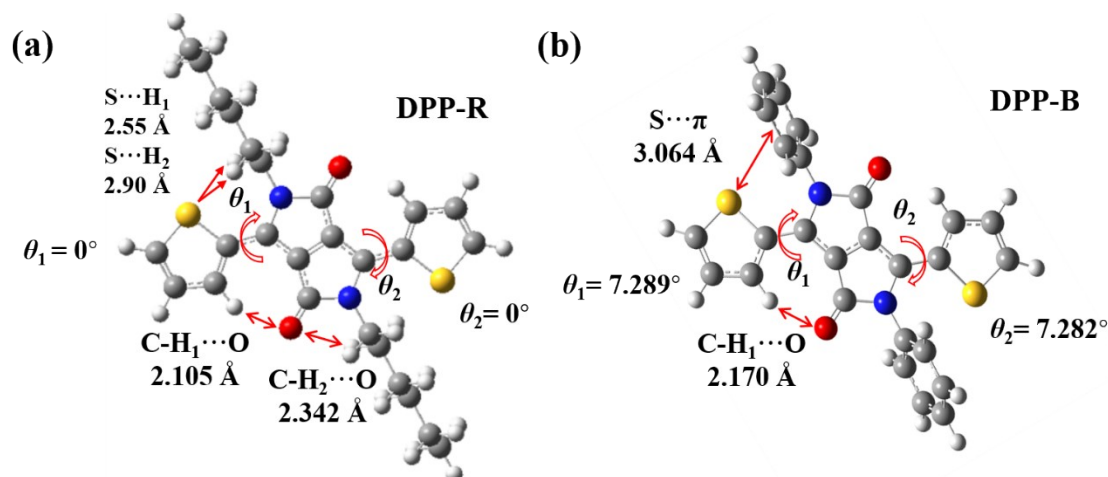


Fig. S7 1D conductance histograms for DPP-R at the concentration of 0.5 mM (a), 1 mM (b) and 2 mM (c) in TCB.

## S4 Optimization and analysis of molecular structures

We optimized the DPP structures using DFT/B3LYP/6-311\*G(d,p). **Fig. S8a** shows that the sulfur atoms will form S $\cdots$ H interactions (2.55 and 2.90 Å) with the hydrogen atoms on the alkyl groups of DPP-R. In addition, the carbonyl oxygens on the DPP backbone will form C–H<sub>1</sub> $\cdots$ O and C–H<sub>2</sub> $\cdots$ O interactions. The dihedral angles ( $\theta$ , as shown in **Fig. S8a**) are 0°. As shown in **Fig. S8b**, with the rigid phenyl substitution, the resulting large steric hindrance leads to a larger dihedral angle of DPP-B (see  $\theta = 7.289^\circ/7.282^\circ$ ). Notably, the distance from the sulfur atom to the center of phenyl groups is 3.064 Å. According to the literature, this special conformation can have S $\cdots$  $\pi$  weak interaction.<sup>4</sup> In the following, we performed NCI analysis using reduced density gradient (RDG) to visualize the S $\cdots$  $\pi$  interaction.



**Fig. S8** The optimized conformations of DPP-R and DPP-B.

**Table. S2** Summary of molecular junction distances.

Molecule	Theoretical Calculation (S-S) (nm)	Conductance measurement (nm)
DPP-R	0.91	$0.83 \pm 0.21$
DPP-B	0.92	$0.88 \pm 0.20$

## S5 Cyclic voltammetry (CV), absorption spectrum and energy level

The oxidation initiation potential of DPP-R and DPP-B is measured by cyclic voltammetry (**Fig. S9a**). According to the equation of  $\text{HOMO} = -e(E_{\text{ox}} + 4.8 - E_{\text{Fc}})$  (eV), (where  $e$  is the electron charge,  $E_{\text{Fc}} = 0.53$  eV, it was measured in the same condition),<sup>5</sup> the HOMO energy levels for both DPP-R and DPP-B are estimated to be -5.24 eV. The optical band gap ( $E_{\text{g}}^{\text{opt}}$ ) of DPP-R and DPP-B can be obtained through  $E_{\text{g}} = 1240/\lambda_{\text{abs}}$  (where  $\lambda_{\text{abs}}$  is the absorption threshold of UV-vis), which are calculated to be 2.16 and 2.19 eV, respectively (**Fig. S9b**). Then LUMO levels can be calculated according to  $E_{\text{LUMO}} = E_{\text{HOMO}} + E_{\text{g}}^{\text{opt}}$ . As shown in **Fig. S9c**, the HOMO level of the molecule is closer to the Fermi level than their LUMO level, which means that HOMO functions as the dominant charge transport channel for DPP-R and DPP-B (**Fig. S9c**).<sup>6</sup>

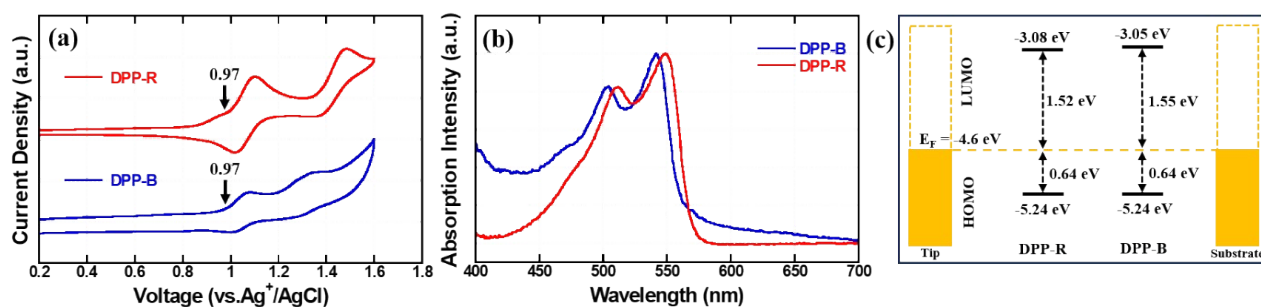


**Fig. S9** (a) The cyclic voltammetry curves of DPP-R and DPP-B in dichloromethane. (b) The UV-vis absorption spectra of DPP-R and DPP-B in dichloromethane solutions ( $10^{-5}$  M). (c) The experimental energy level diagram of DPP-R and DPP-B relative to the Au Fermi energy level.

## S6 AIM analysis by Multiwfn

The optimized molecular structures of DPP-R and DPP-B were performed by Multiwfn, and then the C—H<sub>1</sub> · · · O interaction was analyzed using AIM (Atoms in Molecules). The bond critical points (BCP, referring to first-order saddle points on the electron density scalar field) correspond to the C—H<sub>1</sub> · · · O interaction in DPP-R and DPP-B, and the value of this point (electron density,  $\rho$ ) is utilized to describe the intensity of the corresponding two-atomic interaction.

## S7 Summary of the photophysical and electrochemical of DPP-R and DPP-B

Table S3 Summary of the photophysical and electrochemical of DPP-R and DPP-B

molecule	$\theta_1/\theta_2^a$ (°)	DFT Calculation (eV)			CV & UV-vis (eV)			C-H <sub>1</sub> · · · O interaction $\rho$ (a.u.) <sup>e</sup>
		HOMO	LUMO	$E_g^{cal}$	HOMO <sup>b</sup>	LUMO <sup>c</sup>	$E_g^{optd}$	
DPP-R	0/0	-5.14	-2.72	2.46	-5.24	-3.08	2.17	0.01911
DPP-B	7.289/7.282	-5.17	-2.64	2.53	-5.24	-3.05	2.19	0.01754

<sup>a</sup> Optimized dihedral angles. <sup>b</sup> HOMO estimated from the onset of the oxidation potential [vs. ferrocene (Fe)]. <sup>c</sup> LUMO calculated from HOMO and  $E_g^{opt}$ . <sup>d</sup> Optical energy band gaps ( $E_g^{opt}$ ) estimated from the absorption edge. <sup>e</sup> Electron densities ( $\rho$ ) of BCP.

## S8 Cyclic voltammetry and Mulliken charge density of DPP-R and DPP-B.

S · · ·  $\pi$  interactions makes S atoms being more abundant of charge and vulnerable to be oxidized.<sup>7</sup> Then, DPP-R, DPP-B, and the original DPP was measured by cyclic voltammetry (CV), with the CV result showed in Fig. S10. We find that both DPP-R and DPP-B have a lower oxidation potential than the unmodified DPP. Regarding DPP-R, this can be understood in term of the electron-donating nature of hexyl groups which delocalize more charge to DPP. However, no report has demonstrated that the aromatic benzene ring showed electron-donating ability. Then the reduction of oxidation onset for DPP-B should not arise from the same reason, alternatively S · · ·  $\pi$  interaction might increase the electron density of S atom via through-space coupling. This can be further verified by the Mulliken charge density obtained from molecular simulations (Fig. S11 showing the electron on S for DPP-R and DPP-B increased as compared to DPP).<sup>8</sup> Thus, the existence of S · · ·  $\pi$  interactions can be confirmed by these evidences.

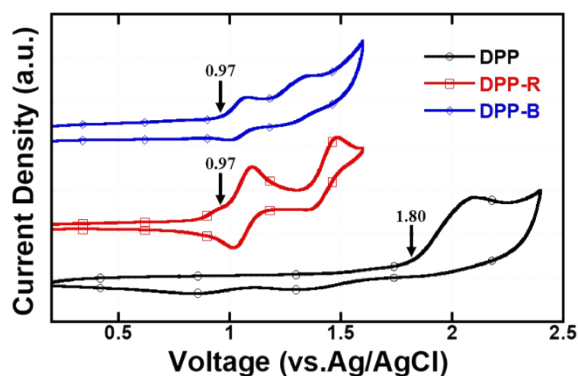


Fig. S10 The cyclic voltammetry curves of DPP, DPP-R and DPP-B in DCM.

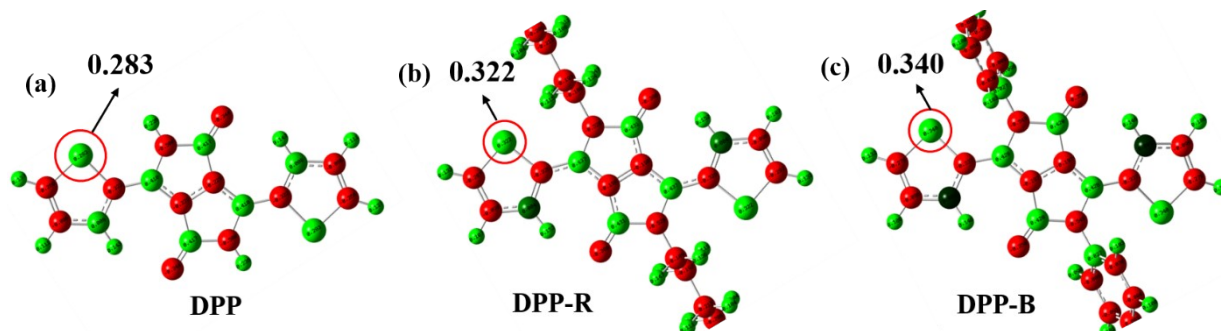
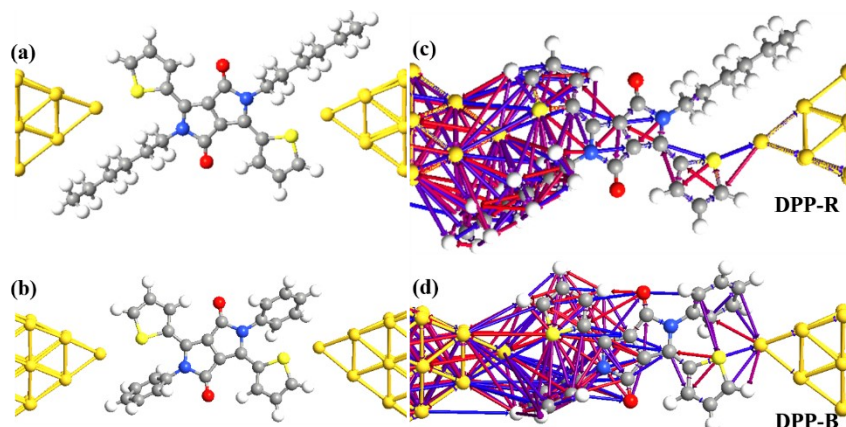


Fig. S11 Charge distributions of DPP, DPP-R and DPP-B.

## S9 Au—S binding configuration and transmission pathway for DPP-R and DPP-B

The system was calculated by the density functional theory (DFT) method. The ground state geometry of DPP-R and DPP-B in the gas phase was optimized using B3LYP/6-311\*G(d,p) basic set. Then, the optimized structures based on 6-311\*G(d,p) were inserted between two electrodes to form molecular junctions. **Fig. S12** illustrates the representative model of the molecular junction with Au/molecule/Au structure. The optimized geometries and transport behaviors of the molecular junctions were carried out using DFT-NEGF under the Atomistix Toolkit (ATK) package. The generalized gradient approximation (GGA-PBE) was used to calculate the electron exchange and correlation. The single zeta polarization (SZP) basis set for the Au atom, and the double zeta polarization (DZP).basis set were employed for C, H, O, N, and S atoms. In the optimization process, the scattering area including central organic molecule was relaxed completely, while the coordinates of the electrode atoms were frozen.



**Fig. S12** (a, b) Single molecular junction geometries for DPP-R and DPP-B. (c, d) The calculated electron transport pathways for DPP-R and DPP-B, and the thresholds were set as  $5 \times 10^{-5}$ .

## Reference

- (1) S. Ying, M. Chen, Z. Liu, K. Zhang, Y. Pan, S. Xue, W. Yang. *J. Mater. Chem. C*, 2016, **4**, 8006-8013. doi:10.1039/C6TC02761J
- (2) W. Jiang, Z. Liu, D. Zhu, W. Zheng, L. Chen, X. Zhang, G. Zhang, Y. Yi, L. Jiang, D. Zhang. *Angew. Chem. Int. Ed.*, 2021, **60**, 10700-10708. doi: 10.1002/anie.202102131
- (3) S. Li, E. R. Jira, N. H. Angello, J. Li, H. Yu, J. S. Moore, Y. Diao, M. D. Burke, C. M. Schroeder, *Nat. Commun.*, 2022, **13**, 2102. doi: 10.1038/S41467-022-29796-2
- (4) P. Chakrabarti, R. Bhattacharyya, *Prog. Biophys. Mol. Biol.*, 2007, **95**, 83. doi:10.1016/j.pbiomolbio.2007.03.016
- (5) Y. C. Li, Z. H. Wang, X. L. Li, G. Z. Xie, D. C. Chen, Y. -F. Wang, C. -C. Lo, A. Lien, J. B. Peng, Y. Cao, S. -J. Su, *Chem. Mater.*, 2015, **27**, 1100. doi: 10.1021/cm504441v
- (6) L. Yu, Z. Wang, H. J. Chen, J. Guo, M. Y. Zhang, Y. C. Liu, J. He, S. Chang, *ACS Appl. Energy Mater.*, 2020, **3**, 3410. doi: 10.1021/acsanm.0c00161
- (7) W. J. Chung, M. Ammam, N. E. Gruhn, G. S. Nichol, W. P. Singh, G. S. Wilson, R. S. Glass, *Org. Lett.*, 2009, **11**, 397-400. doi: 10.1021/ol802683s
- (8) Q. Ai, J. Zhou, J. Guo, P. Pandey, S. Liu, Q. Fu, Y. Liu, C. Deng, S. Chang, F. Liang, J. He, *Nanoscale*, 2020, **12**, 17103-17112. doi: 10.1039/D0NR03360J